Macromolecules
ARTICLE

Macromolecules **2010**, *43*, 8637–8644 **8637**
DOI: 10.1021/ma1009885

Single Helix to Double Gyroid in Chiral Block Copolymers

Chun-Ku Chen,[†] Han-Yu Hsueh,[†] Yeo-Wan Chiang,[†] Rong-Ming Ho,*[,†] Satoshi Akasaka,[‡] and Hirokazu Hasegawa*[,‡]

[†]*Department of Chemical Engineering, Nationsal Tsing-Hua University, Hsinchu 30013, Taiwan, and* [‡]*Department of Polymer Chemistry, Graduate School of Engineering, Kyoto University, Nishikyo-ku, Kyoto, 615-8510, Japan*

Received May 4, 2010; Revised Manuscript Received August 17, 2010

ABSTRACT: An order−order phase transition of chiral block copolymers (BCPs*) from single helix to double gyroid (H* → G) through a nucleation and growth process was demonstrated. The H* and G phases can be obtained by solution casting from fast and slow solvent evaporation, respectively, suggesting that the H* phase is a metastable phase. Consequently, the coexistence of H* and G phases can be found in the solution-cast samples from intermediate solvent evaporation. To truly examine the transition mechanism of the H* → G, electron tomography was carried out to directly visualize the morphological evolution in real space, in particular, the transition zone at interface. Unlike the mechanisms for the transitions of block copolymers (BCPs) by considering the interdomain spacing matching, a significant mismatch in the lattices for the H* → G was found. Consequently, the transition may require an adjustment on the geometric dimensions to justify corresponding lattice mismatch. As a result, the morphological observations from electron tomography offer new insights into BCP phase transitions.

Introduction

Block copolymers (BCPs) consisting of chemically different components have been extensively studied because of their abilities to self-assemble into various ordered phases such as sphere (S), cylinder (C), gyroid (G), and lamellae (L) according to various compositions (i.e., volume fractions).[1−3] Among all of self-assembled phases, gyroid is one of the most appealing morphologies for applications in nanotechnology[4−11] because of its unique texture with a matrix and two continuous networks in three-dimensional (3D) space. The applications, such as photonic crystals,[4] separation membranes,[5] membrane reactors,[6−10] and solar cells,[11] have all been well demonstrated. Order−order phase transitions from hexagonally perforated layer (HPL) phase,[12,13] sponge phase,[14] C phase,[15−18] or L phase[12,13,19,20] to G phase have been found; the transition mechanism was demonstrated to be a nucleation and growth process.[21−23] The phase transition may take action upon thermal annealing and temperature variation. Hashimoto et al. investigated the ordering dynamics and mechanism of poly(styrene)-*b*-poly(isoprene) BCPs by changing temperatures from order−disorder transition temperature. It revealed that a nucleation occurs homogeneously and then generates a highly anisotropic shape of grains composed of L phase.[21] Lodge et al. examined the kinetics of grain growth of concentrated poly(styrene)-*b*-poly(isoprene) BCP solutions during thermally induced phase transitions. As observed, a HPL → G phase transition from the growth front velocities of grains resulting from order−order phase transformation could be reliably obtained.[22] Thomas et al. prepared an isoprene-rich poly(styrene)-*b*-poly(isoprene)-*b*-poly(styrene) BCP having G phase via roll casting and annealing. Upon annealing, the equilibrium G phase nucleates and grows from C phase, with the [111] direction along the cylindrical axes of C phase (i.e., the roll cast direction).[23]

*To whom correspondence should be addressed: Tel 886-3-5738349; Fax 886-3-5715408; e-mail rmho@mx.nthu.edu.tw.

Recently, chiral block copolymers (BCP*) comprising chiral entities were designed to fabricate helical architectures (i.e., twisted morphologies) from self-assembly.[24−30] A new helical phase (H*) with *P*622 symmetry was discovered in the self-assembly of poly(styrene)-*b*-poly(L-lactide) (PS−PLLA) BCPs*.[30] Unique transmission electron microscopy (TEM) projection images comprising twisted morphologies in the self-assembled nanostructure of the PS−PLLA with a volume fraction of PLLA (f_{PLLA}^{v}) = 0.34 prove the presence of a H* phase, whereas no such projection image can be found in racemic BCPs (that is, poly(styrene)-*b*-poly(DL-lactide) (PS−PLA)).[31] Hexagonally packed, interdigitated PLLA helical domains in a PS matrix were directly visualized by electron tomography. For PS−PLLA with (f_{PLLA}^{v}) = 0.65, a core−shell cylinder phase with helical sense control (CS*), in which PS microdomains appear as shells and PLLA microdomains appear as a matrix and cores, could be found.[26] Furthermore, similar to the phase behavior of metastable PL phase, phase transitions from the H* phase to stable phases such as C and G phases upon thermal annealing were found, indicating that the H* phase is a long-lived metastable phase. The formation of the H* phase is attributed to the slow relaxation of long, highly entangled chains during self-assembly. A phase diagram of the PS−PLLA block copolymer has been developed to establish the regions of phase formation in terms of composition and molecular weight in our previous study.[30]

In addition to phase transitions resulting from thermal annealing, temperature variation,[12,13] shearing,[15−18] and solvent evaporation[32,33] could also be utilized to induce phase transitions. Different from the control of phase transitions via the thermal annealing process, order−order phase transitions could be achieved simply by controlling the solvent evaporation rate for solution-cast samples. To reach the formation of equilibrium morphology, the controlling process is to reduce the evaporation rate so as to give polymer chains enough mobility and time to self-assemble as a state close to an equilibrium phase. Libera and co-workers described that morphological development in solvent-cast poly(styrene-*b*-butadiene-*b*-styrene) (SBS) triblock copolymer thin films (30 wt %

Published on Web 09/30/2010

PS) as a function of solvent evaporation rate. Alternate and metastable morphologies were generated under kinetically constrained conditions. A microphase-separated microstructure with no long-range order was generated from fast evaporation. Intermediate evaporation generated hexagonally packed (vertical) PS cylinders in a PB matrix with the cylinder axis perpendicular to the film plane. Very slow solvent evaporation produced a fully in-plane cylinder microstructure.[32] He and co-workers reported the observation of inverted phases in a SBS triblock copolymer by solvent induced order−disorder phase transition. Kinetic control with different evaporation rate should correspond to the effective interaction parameter of the polymer solution in the cast film and the number of "blobs" of size equal to the correlation length one block copolymer chain contains.[33]

The self-assembly of BCPs for the formation of well-defined phases is usually carried out from melt or solution. For the phase transitions induced by thermal annealing, it is usually carried out at temperature above the glass transitions of constituted blocks for long time. It is noted that the transitions of various metastable phases to thermodynamically stable phase might be reached by thermal annealing while the initial morphology is a metastable phase. Accordingly, the forming morphologies resulting from thermal annealing can also be a kinetic one. To reach the equilibrium morphology, the time for thermal annealing is a controlling factor. By contrast, phase transitions induced by solvent evaporation can be achieved under ambient conditions which alleviates the degradation problem at high temperature for thermal annealing for a long time. Moreover, because of the less entanglement for the BCP chains in solution, the formation of phases from microphase separation would be suitably controlled so as to create well-defined phases with large-scale orientation for the examination of transition mechanism. Consequently, the transition state might be caught by controlling solvent evaporation for solution-cast samples.

To investigate the phase transitions of BCPs, indirect observation of BCPs was generally performed by small-angle X-ray scattering (SAXS), a very powerful tool to get structural information averaged over a large sample volume but incompetent to provide detailed structural analysis. To address this problem, direct TEM imaging of phase transitions were carried out.[13,16] However, only limited information can be obtained from these TEM images which are 2D projections of 3D objects and therefore cannot reveal 3D information on complex structures. Electron tomography (i.e., 3D TEM) was developed to directly observe 3D nanostructures of BCPs.[34,35] In this study, we aim to examine the mechanism of phase transition from single helix to double gyroid through the control of solvent evaporation rate for solution casting. SAXS is carried out to examine the averaged structural information the phase transition. Electron tomography is utilized to directly visualize the transition. The phase transition from H* phase to G phase (H* → G) is observed for the first time, demonstrating the geometric rearrangement from single-helix H* phase to double-helix G phase. As a result, the morphological observations from electron tomography offer new insights into BCP phase transitions.

Experimental Section

Synthesis. PS−PLLA BCP* was prepared by a sequential living polymerization using a double-headed initiator. Detailed synthetic routes of the PS−PLLA samples were described in our previously published results.[26] The number-average molecular weight and the molecular weight distribution (i.e., polydispersity index) of PS block were determined by GPC. The polydispersity index (PDI) of PS−PLLA was determined by GPC, and the numbers of L-LA repeating units vs styrene repeating units were determined by ^{1}H NMR analysis. The number-average molecular weights of PS and PLLA blocks as well as the PDI of BCP* are 34 000 g mol^{-1}, 27 000 g mol^{-1}, and 1.21, respectively. The volume fraction of PLLA, $f_{PLLA}{}^{v}$, is thus calculated as 0.39 by assuming the densities of PS and PLLA are 1.02 and 1.248 g cm^{-3}, respectively.

Sample Preparation. PS−PLLA BCP* was first dissolved in dichloromethane (CH_2Cl_2) at a concentration of 10 wt %. After the PS−PLLA BCP* was completely dissolved in dichloromethane, the solution was filtrated through a filter with 0.45 μm pores to remove impurities. The solution was then transferred into a vial for solution casting; the evaporation rate was controlled by sealing the vial with aluminum foil having punch holes. Bulk samples from different evaporation rates were prepared by adjusting the amount of holes and corresponding size for solution casting. To qualitatively examine the effect of solvent evaporation rate on self-assembled phases from microphase separation at ambient condition (~25 °C), results from three samples denominated as samples from fast, intermediate, and slow evaporation were demonstrated. The solution-cast sample obtained through solvent evaporation without sealing was referred to sample from fast evaporation. The solution-cast sample from slow evaporation was obtained by sealing the vial with aluminum foil having one punch hole (diameter ~0.5 mm). Accordingly, as the sealed aluminum foil with ten punch holes, the solution-cast sample was referred to sample from intermediate evaporation. The solvent evaporation for casting was carried out for approximately 3 h, 5 days, and 2 weeks for the samples from fast, intermediate, and slow evaporation, respectively. The obtained samples were further dried in vacuum oven for 3 days at 50 °C to remove the residual solvent. Subsequently, the samples were thermally treated at 180 °C (temperature with microphase-separated melt) for 3 min to eliminate PLLA crystalline residues. After thermal treatment, the samples were quenched to ambient condition for SAXS experiments and then sectioned by ultramicrotome (thickness ~100 nm) for TEM observation. The microsections were stained by exposing to the vapor of a 4% aqueous RuO_4 solution for 1 h. The RuO_4 attacks the double bonds in PS blocks, rendering those microphase-separated domains dark in TEM due to the mass−thickness contrast. The samples for electron tomography were treated with sol−gel reaction after hydrolysis so as to enhance the contrast and resolution of reconstructed 3D images.[28]

Sol−Gel Procedure. PLLA blocks of the thermally treated PS−PLLA bulk samples were removed by hydrolysis at which 0.5 M basic aqueous solution was prepared by dissolving 2 g of sodium hydroxide in a 40/60 (by volume) solution of methanol/water for the hydrolysis of PLLA blocks. After hydrolysis for 3 days, the hydrolyzed samples were rinsed by using mixed solution of DI water and methanol and then used as templates for following sol−gel reaction. Silica precursor mixture was introduced into the PS templates by immersing the templates in TEOS/$HCl_{(aq)}$(0.1 M)/methanol mixture (weight fraction of TEOS/$HCl_{(aq)}$(0.1 M)/methanol = 10/1/25) with stirring at room temperature for 24 h and then treated under controlled humidity at 40 °C for 48 h. After drying, PS/SiO_2 nanocomposite samples were prepared.[28]

X-ray Experiments. SAXS experiments were conducted at the synchrotron X-ray beamline X27C at the National Synchrotron Light Source (NSLS) in Brookhaven National Laboratory (BNL). The wavelength of X-ray beam was 0.1371 nm. The scattering angle of SAXS pattern was calibrated using silver behenate, with the first-order scattering vector q^* ($q^* = 4\pi\lambda^{-1}$ sin θ, where 2θ is the scattering angle) of 1.076 nm^{-1}.

Transmission Electron Microscopy (TEM). Bright-field TEM images were obtained using the mass−thickness contrast with a JEOL JEM-2100 LaB6 transmission electron microscope (at an accelerating voltage of 200 kV).

Electron Tomography. PS−PLLA bulk samples after sol−gel reaction were sectioned by a Leica Ultramicrotome (thickness ~100 nm) at room temperature for electron tomography. The microsections were collected on copper grids (100 mesh) covered by a poly(vinyl formal) membrane. For the requirement of

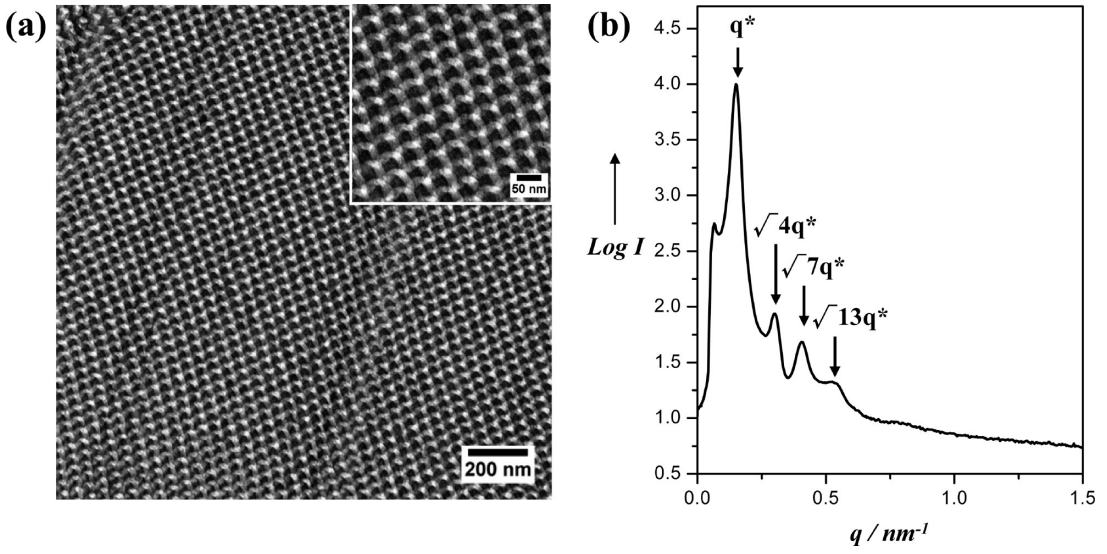

Figure 1. (a) TEM micrograph and (b) corresponding 1D SAXS profile of PS−PLLA solution-cast sample from fast evaporation. Inset shows the enlarged image.

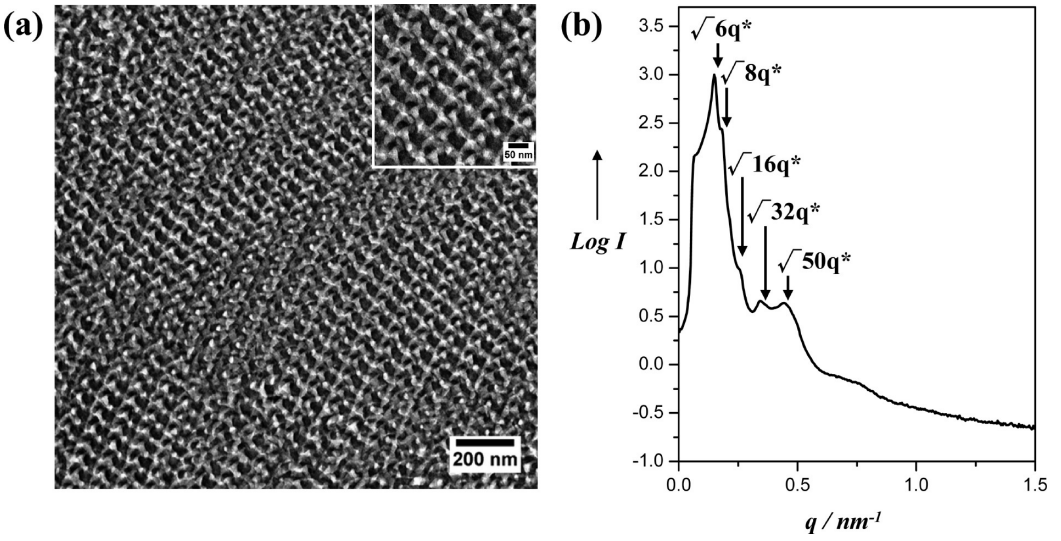

Figure 2. (a) TEM micrograph and (b) corresponding 1D SAXS profile of PS−PLLA solution-cast sample from slow evaporation. Inset shows the enlarged image.

image alignment to reconstruct 3D imaging, fiducial gold markers (diameter 10 nm, purchased from Polysciences, Inc.) were used and homogeneously distributed onto the microsections with the right amount of markers to observe grain boundaries. Then, a series of 71 TEM projection images were collected from −70° to +70° tilt angles at an angular interval of 2° on a JEOL (JEM-2100) TEM operated at 200 kV. Images were recorded on a Gatan CCD camera. Alignment of the tilt series and 3D reconstruction were performed by using IMOD software. The reconstructed volume was then filtered by a $5 \times 5 \times 5$ median filter for noise reduction. Analyze 4.0 (AnalyzeDirect) was then used to trim the filtered volume keeping only a volume of interest for further analysis. Finally, 3D analyses such as binarization, segmentation, and visualization of the volume of interest were achieved using Analyze 4.0.

Results and Discussion

Formation of H* and G Phases. Figure 1a shows the TEM projection images of solution-cast sample from fast evaporation. Because of RuO_4 staining, the PS microdomain appears dark whereas the PLLA microdomains appear bright. The crescent image is resulted from the projection of PLLA helices slightly tilting from the helical central axis in a PS matrix so as to suggest the formation of H* phase.[24] The helical pitch length can be determined as 140 nm, consistent with the result estimated by experiments and simulations as reported by our group previously.[30] (see Supporting Information for simulated projection images of H* phase at different tilt angles). Figure 1b shows corresponding 1D SAXS profile and the reflection peaks are found to occur at the q^* ratios of $1:\sqrt{4}:\sqrt{7}:\sqrt{13}$, indicating that those PLLA helices are hexagonally packed. The interdomain spacing of $(100)_{H^*}$ (i.e., $d_{(100)H^*}$) was determined as ~42.1 nm according to the primary reflection.

Figure 2a shows the TEM projection image of sample from slow evaporation. The [220] projection of the G phase was found under TEM observation (see Supporting Information for 3D graphic model of G phase and typical cross sections of its planes), and the corresponding 1D SAXS profile (Figure 2b) shows that the reflection peaks are found to occur at the q^* ratios of $\sqrt{6}:\sqrt{8}:\sqrt{16}:\sqrt{32}:\sqrt{50}$ which further demonstrates the formation of G phase. Gyroid-forming BCPs with constant thickness predicts strong reflections at $\sqrt{6}$ and $\sqrt{8}$ only, and all

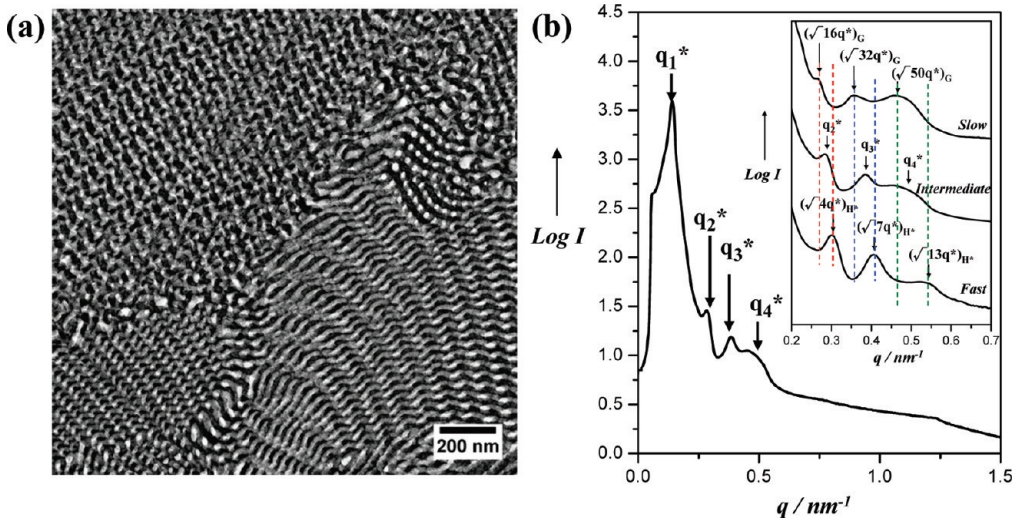

Figure 3. (a) TEM micrograph of PS−PLLA solution-cast sample from intermediate evaporation and (b) corresponding 1D SAXS profile. Inset shows the 1D SAXS profiles of PS−PLLA samples from fast, intermediate, and slow evaporation.

other reflections are relatively weak.[39] Some reflections are apparently canceled by the structure factor of the gyroid morphology in the pure diblock copolymer. This is very common in diblock copolymer systems different from triblock copolymer systems.[40] The interdomain spacing of $(211)_G$ (i.e., $d_{(211)G}$) was determined as ~40.1 nm according to the primary reflection. The results indicate that the formation of H* and G phases can be achieved by simply controlling the solvent evaporation rate for solution casting. From our previous study, the stable (equilibrium) morphology of the block copolymer studied here would be a gyroid phase but not a lamellar one. Also, phase transition from the H* phase to gyroid phase could be found after reasonably high-temperature annealing for long time, suggesting that the helical phase is a long-lived metastable phase.[30] It is reasonable to suggest that the metastable H* phase can be kinetically trapped as the evaporation rate for solution casting is fast enough. Namely, given enough time under condition of relatively long relaxation time (i.e., slow evaporation), the PS−PLLA BCP* chains with enough mobility and time are able to self-assemble as a thermodynamically stable phase (i.e., G phase) through a kinetic process. By contrast, with shorter time for relaxation (i.e., fastest evaporation rate), self-assembled morphologies might be frozen in to form metastable phase such as H* phase due to the low mobility of long polymer chains for self-assembly. As a result, the transition stage (i.e., the coexistence of the H* and G phases) can be caught once the time for self-assembly (that is the evaporation time) is in between these two conditions. Accordingly, it is much more efficient and reliable to acquire the coexistence of two phases by controlling solvent evaporation rate in film casting process.

Order−Order Phase Transition of H* → G. To acquire the event of the H* → G, cast sample from intermediate evaporation was obtained at which the coexistence of H* and G phases should be identified. As shown in Figure 3a, a duplex phase containing PLLA helices (lower right in Figure 3a) and PLLA gyroid networks (upper left in Figure 3a) in a PS matrix can be found under TEM observation. The corresponding 1D SAXS profile is shown in Figure 3b. The reflection peaks in Figure 3b are denoted as q_1*, q_2*, q_3*, and q_4*, and no specific q* ratio among these four peaks can be identified. This is attributed to the coexistence of the reflections of H* phase (Figure 1b) and G phase (Figure 2b) so as to cause the shifting of the peak positions (as shown in the inset of Figure 3b). Conversely, the q value of q_2* is in between that of $(\sqrt{4}q^*)_{H^*}$ and $(\sqrt{16}q^*)_G$, the q value of q_3* is in between that of $(\sqrt{7}q^*)_{H^*}$ and $(\sqrt{32}q^*)_G$, and the q value of q_4* is in between that of $(\sqrt{13}q^*)_{H^*}$ and $(\sqrt{50}q^*)_G$ (inset in Figure 3b). Consequently, the 1D SAXS results further demonstrate the coexistence of H* and G phases in the solution-cast sample from intermediate evaporation, consistent with the results from TEM observations (Figure 3a).

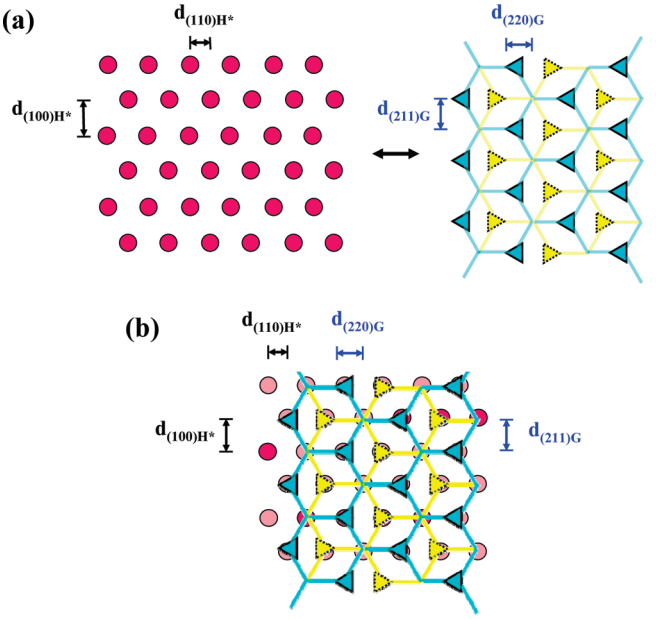

Figure 4. Illustrations of H* → G: (a) the transition is nucleated from $(110)_{H^*}$ plane and subsequently grows to form $(220)_G$ plane and (b) the transition is nucleated from helical central axis and subsequently grows along $[111]_G$ through a nucleation and growth process. Projections are along the helical central axis and [111] direction of the cubic unit cell. Cyan and yellow lines denote two independent gyroid networks constructed from 3-fold connectors. Cyan and yellow triangular elements indicate the left- and right-handed helices of gyroid networks.

Examination of H* → G through Electron Tomography. Various transition mechanisms with respect to C → G have been proposed by many research groups through experimental observations[15−18] or theoretical studies.[36−38] There is a consensus that the phase transition between C → G has an epitaxial relationship at which the phase transform might conduct from the ends of cylindrical axes via the $(001)_C$ to

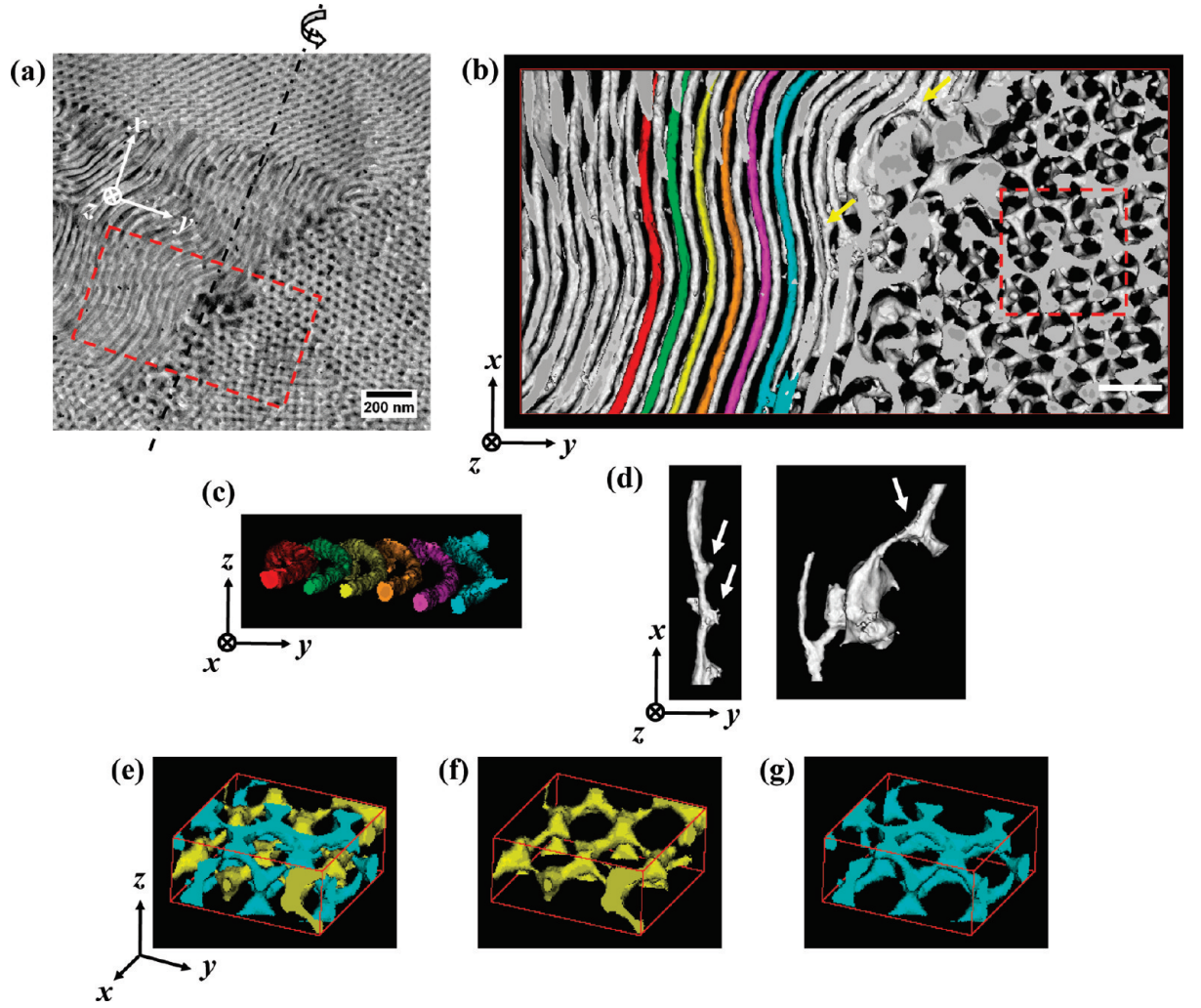

Figure 5. (a) TEM image, tilt angle is 0°, extracted from a tilt series of 71 micrographs. Helical and gyroid phases are observed as well as gold fiducial markers used for image alignment. Dashed line: tilt axis along which the sample was rotated ±70°. Rectangle red dashed line box: position of the reconstructed volume presented in (b). (b) Visualization of a helical/gyroid grain boundary: original portion of the TEM micrograph corresponding to the box area of (a). The scale bar represents 100 nm. (c) The reconstructed helical nanostructure in (b) viewing along the helical axes. (d) The reconstructed microdomains in transition region as pointed out by yellow arrows in (b). White arrows indicate the 3-fold junction characteristic of the gyroid networks. (e) The reconstructed gyroid networks in the rectangle red dashed line box of (b). (f) and (g) represent the individual gyroid networks of (e).

$(111)_G$. On the basis of 1D SAXS results, the correspondence in $d(100)_{H^*}$ and $d(211)_G$ can be determined by considering the interdomain spacing matching (i.e., $d(100)_{H^*} \sim d(211)_G$) for phase transition. On the basis of the model of the phase transition between C → G, it is intuitive to suggest that the helices of $(001)_{H^*}$ transform to $(111)_G$ networks from the ends of helical axes so that the phase transition between H* → G has an epitaxial relationship between the $(110)_{H^*} \rightarrow (220)_G$ in a cubic lattices. It is intuitive to suggest that the H* → G is nucleated from $(110)_{H^*}$ plane and subsequently grows to form $(220)_G$ plane (Figure 4a) or nucleates from helical central axis and subsequently grows along $[111]_G$ (Figure 4b) through a nucleation and growth process.[36] Accordingly, the helices of H* phase transform to G networks from the side of the helices. To truly examine the transition mechanism of H* → G, electron tomography was then carried out to visualize the morphological evolution in real space, in particular, the transition zone at interface. The solution-cast sample from intermediate evaporation which possesses the coexistence of H* and G phases was treated with sol−gel reaction, and subsequently the PS/SiO_2 nanocomposite sample can be prepared.[28] Note that according to our previous work[28] the templated nanostructures remained, and the contrast and resolution of reconstructed 3D images could be significantly improved after the sol−gel process.

Figure 5a shows the projection image (tilt angle is 0°) of the PS/SiO_2 microsection without RuO_4 staining. In contrast to Figure 3a, similar projection image of the coexistence of H* (upper left in Figure 5a) and G phases (lower right in Figure 5a) can be observed. Notably, the contrast is inversed because PLLA blocks are removed completely by hydrolysis and SiO_2 is loaded by the sol−gel process. Those helices would transform to gyroid networks by passing through a transition region (as shown in the rectangle red dashed line box in Figure 5a). Figure 5b−g displays reconstructed 3D images after binarization and segmentation. On the basis of reconstructed images (Figure 5b), it is interesting to recognize that coherent G phase can only be identified on the sides of H* phase (i.e., $(110)_{H^*}$; see Figure 7a for details) but never at the ends of helices (i.e., $(001)_{H^*}$). This might be attributed to larger transitional interface along $[110]_{H^*}$ (i.e., perpendicular to helical central axis of H*) to $[211]_G$ (i.e., perpendicular to helical central axis of G) than along $[00\ L]_{H^*}$ (i.e., parallel to helical central axis of H*) to $[111]_G$ (i.e., parallel to helical central axis of G) so as to compensate the transition energy from single-helix H* phase to double-helix G phase

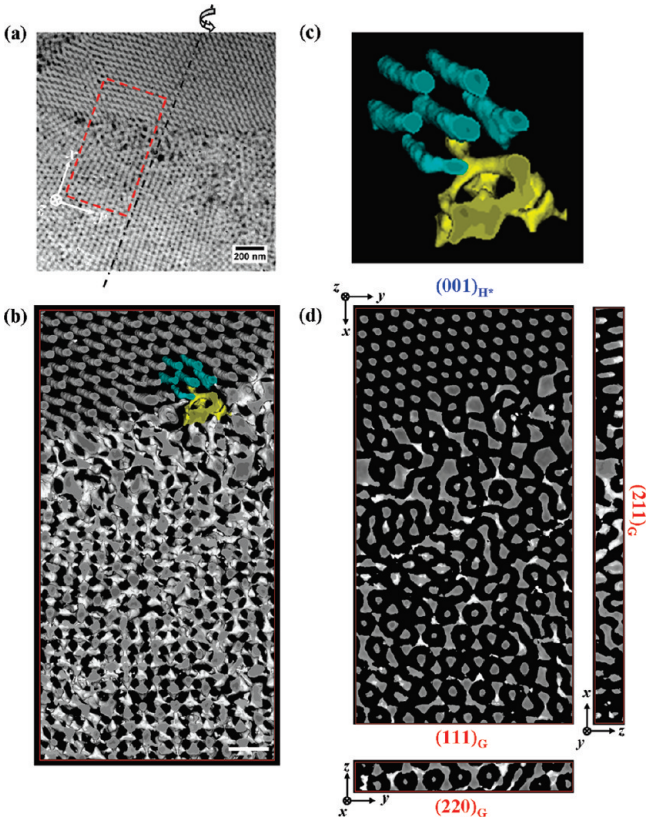

Figure 6. (a) TEM image, tilt angle is 0°, extracted from a tilt series of 71 micrographs. Helical and gyroid phase are observed as well as gold fiducial markers used for image alignment. Dashed line: tilt axis along which the sample was rotated ±70°. Rectangle red dashed line box: position of the reconstructed volume presented in (b). (b) Visualization of a helical/gyroid grain boundary: original portion of the TEM micrograph corresponding to the box area of (a). The scale bar represents 100 nm. (c) The enlarged image of the microdomains after segmentation in (b). (d) Orthogonal digital slices (10 nm for the $x-y$ section; 11 nm for the $z-y$ section; 12 nm for the $x-z$ section) of the reconstructed 3D images.

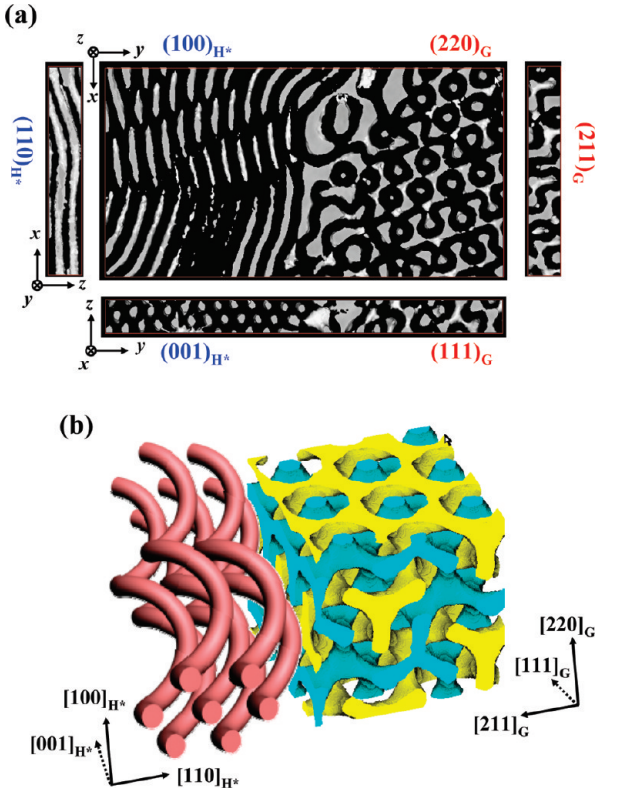

Figure 7. (a) Orthogonal digital slices (11 nm for the $x-y$ section; 23 nm for the $z-y$ section; 19 nm for the $x-z$ section of the G phase; 55 nm for the $x-z$ section of the H* phase) of reconstructed 3D images. (b) Relative geometric arrangement in 3D space of single-helix H* phase and double-helix G phase.

and result in preferred occurrence of the transition from $(110)_{H^*}$. Figure 5c clearly shows the orderly packed helices viewing along the helical central axis. Moreover, the $(110)_{H^*}$ transfers to the $(211)_G$ phase from the side of the helices by passing through a transition region; outer helices (i.e., the pink and cyan helices in Figure 5c) gradually deform and stretch to grow branches as close to the transition region. Subsequently, growing branches gradually transform to gyroid networks through the transition region in which the 3-fold junction character of gyroid networks can be observed (Figure 5d). Finally, well-defined gyroid networks can be found as shown in Figure 5e−g.

Figure 6 shows the reconstructed 3D images of the coexistence phase in which the H* phase is viewing along with slightly tilt from helical central axis (top in Figure 6a). Similarly, a transition region is observed, and the result of the reconstructed 3D images further confirm that the helices transfer to the gyroid networks from the side of the helices by passing through a transition region (Figure 6b). Namely, the G phase is observed only on the side of the helices of the H* phase but never at the ends of the helices. The outer helices gradually grow branches (Figure 6c) as close to the transition region and the growing branches transfer to the gyroid networks by passing through the transition region. The top sequence for H* → G is initiated by forming one junction that eventually pinches off a helix in the center of a 6-fold hexagon and leaves two 3-fold junctions. On the basis of the symmetry in an H* phase and its corresponding long pitch (140 nm), it is a matter of symmetry breaking regardless of helical locus. The transition mechanism of H* → G is similar to that of C → G as reported by Matsen.[36] As the process repeats, H* evolves into G, and the helical pitch length is not responsible for the formation of the left- and right-handed 3-fold coordinated lattices of a G phase (*Ia3d* symmetry). Finally, the well-defined gyroid networks are formed as far from the transition region. Figure 6d shows orthogonal digital slices of the reconstructed 3D images and the transition mechanism are in line with the result of Figure 7a.

Digital slices of different thickness (11 nm for the $x-y$ section; 23 nm for the $z-y$ section; 19 nm for the $x-z$ section of the G phase; 55 nm for the $x-z$ section of the H* phase) are presented in Figure 7a. The results indicate that the nucleation of G phase from H* phase is initiated from the $(110)_{H^*}$ plane and the growth of G phase is followed by $[211]_G$. Accordingly, the transition leads the corresponding geometries of $(110)_{H^*} \rightarrow (211)_G$, $(100)_{H^*} \rightarrow (220)_G$, and $(001)_{H^*} \rightarrow (111)_G$. Furthermore, the $d_{(100)H^*}$ and $d_{(211)G}$ can be calculated as approximately 40.5 and 38.5 nm from the digital slices of the reconstructed 3D images, respectively. To compare with the value of 1D SAXS results, it is about 4% reduction in the interdomain spacing after sol−gel reaction because of the swelling of PS matrix by the sol so as to lead the dimensional change after the formation of dry gel.[28]

Transition Mechanism of H* → G. On the basis of the observation of electron tomography, the relative geometric arrangement in 3D space of single-helix H* phase and double-helix G phase is illustrated in Figure 7b. The results indicate an interesting geometric rearrangement for H* → G.

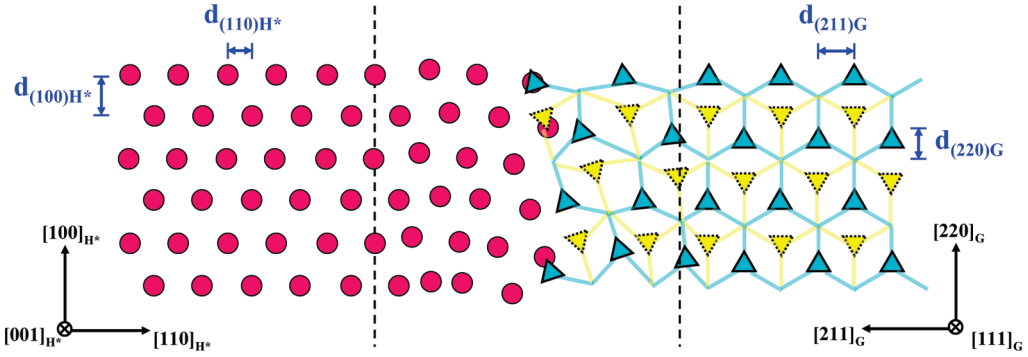

Figure 8. Illustrations of the H* → G: the transition is nucleated from $(110)_{H^*}$ plane and subsequently grows to form the $(211)_G$ plane. Projections are along helical central axis (left) and [111] direction of cubic unit cell (right). Cyan and yellow lines denote two independent gyroid networks constructed from 3-fold connectors. Cyan and yellow triangular elements indicate the left- and right-handed helices of gyroid networks.

Unlike the mechanisms (the suggested nucleation from $(110)_{H^*}$ plane to form $(220)_G$ plane) for the transitions of BCPs by considering the interdomain spacing matching (i.e., $d(100)_{H^*} \sim d(211)_G$), H* → G is nucleated from the $(110)_{H^*}$ plane to form $(211)_G$. As shown in Figure 8, the large difference between $d_{(100)H^*}$ (~42.1 nm) and $d_{(220)G}$ (~34.7 nm) calculated from 1D SAXS results indicates a significant mismatch (~18%) in the lattices for H* → G. Consequently, the transition may require an adjustment on the geometric dimensions to justify corresponding lattice mismatch. The phenomenon was also observed for C → G under shearing.[15,16] The formation of the lattice adjustment in C → G is attributed to the difference in shearing time so that the orientation of cylinders is rotated around the cylinder axis relative to the specimen that transforms into gyroid networks. In the case of H* → G, we speculate that the lattice adjustment is attributed to the transition along helical locus from the single helix of H* phase to the double helix of G phase. Accordingly, the transition region can be identified (Figures 5b and 7a) owing to the necessity of space for lattice adjustment during phase transition. Because of corresponding lattice mismatch for transition, the boundary between the phases is rather disorganized. As evidenced by the results of SAXS and 3D TEM, the geometries of $(110)_{H^*} \rightarrow (211)_G$ and $(100)_{H^*} \rightarrow (220)_G$ resulting from the phase transition with corresponding length scale and unit cell can thus be well-defined.

To conclude, apart from the phase transitions upon thermal annealing and temperature variation, the order−disorder phase transition could result from the control of solvent evaporation. We speculate that the transitions from solution state should experience an order−disorder transition first, and then an order−order transition may take action after further evaporation, similar to the variations in response to the decrease of temperature from the temperature above order−disorder transition temperature.

Also, on the basis of the measured grain sizes of G phases growing from H* phases, we suggest that the order−order phase transition from H* to G phase was carried out through a nucleation and growth process. As observed, the G phase from H* phase shows variation in the grain size, indicating a homogeneous nucleation, and the grain of the G phase appears as an anisotropic shape, further demonstrating the character of the growth of G phase from H* phase through a specific growing plane.

Conclusions

In conclusion, the metastable H* and stable G phases can be obtained by solution casting from fast and slow solvent evaporation, respectively, so that the coexistence of H* and G phase was found in the solution-cast samples from intermediate evaporation. By considering the interdomain spacing matching (i.e., $d(100)_{H^*} \sim d(211)_G$) for phase transition, on the basis of 1D SAXS result, a hypothetic transition mechanism was suggested; the H* → G is nucleated from the $(110)_{H^*}$ plane and subsequently grows to form the $(220)_G$ plane or nucleates from helical central axis and subsequently grows along $[111]_G$. By contrast, an interesting geometric rearrangement of the H* → G was observed through the direct visualization of electron tomography; the H* → G is nucleated from $(110)_{H^*}$ plane to form the $(211)_G$ plane which causes a significant mismatch in the lattices for phase transition. Consequently, the transition may require an adjustment on the geometric dimensions to justify corresponding lattice mismatch. As a result, the morphological observations from electron tomography offer new insights into BCP phase transitions.

Acknowledgment. We thank Prof. Benjamin S. Hsiao of the Chemistry Department, State University of New York at Stony Brook, and Dr. Lixia Rong of the National Synchrotron Light Source at Brookhaven National Laboratory for their help in synchrotron SAXS experiments. The National Synchrotron Radiation Research Center (NSRRC) is appreciated for its assistance in the Synchrotron SAXS experiments. This work is supported by National Science Council (NSC 99-2120-M-007-003).

Supporting Information Available: Detailed experimental procedures for the sample preparation and 3D TEM projection images of the transition mechanism of the H* → G viewing. This material is available free of charge via the Internet at http://pubs.acs.org.

References and Notes

(1) Bates, F. S.; Fredrickson, G. H. *Annu. Rev. Phys. Chem.* **1990**, *41*, 525.
(2) Matsen, M. W.; Schick, M. *Phys. Rev. Lett.* **1994**, *72*, 2660.
(3) Bates, F. S.; Fredrickson, G. H. *Phys. Today* **1999**, *52*, 32.
(4) Edrington, A. C.; Urbas, A. M.; DeRege, P.; Chen, C. X.; Swager, T. M.; Hadjichristidis, N.; Xenidou, M.; Fetters, L. J.; Joannopoulos, J. D.; Fink, Y.; Thomas, E. L. *Adv. Mater.* **2001**, *13*, 421.
(5) Chan, V. Z.-H.; Hoffman, J.; Lee, V. Y.; Latrou, H.; Avgeropoulos, A.; Hadjichristidis, N.; Miller, R. D.; Thomas, E. L. *Science* **1999**, *286*, 1716.
(6) Adachi, M.; Okumura, A.; Sivaniah, E.; Hashimoto, T. *Macromolecules* **2006**, *39*, 6352.
(7) Hashimoto, T.; Nishikawa, Y.; Tsutsumi, K. *Macromolecules* **2007**, *40*, 1066.
(8) Jinnai, H.; Kaneko, T.; Nishioka, H.; Hasegawa, H.; Nishi, T. *Chem. Rec.* **2006**, *6*, 267.
(9) Mao, H. M.; Hillmyer, M. A. *Soft Matter* **2006**, *2*, 57.
(10) Urade, V. N.; Wei, T. C.; Tate, M. P.; Kowalski, J. D.; Hillhouse, H. W. *Chem. Mater.* **2007**, *19*, 768.

(11) Crossland, E. J. W.; Kamperman, M.; Nedelcu, M.; Ducati, C.; Wiesner, U.; Smilgies, D.-M.; Toombes, G. E. S.; Hillmyer, M. A.; Ludwigs, S.; Steiner, U.; Snaith, H. J. *Nano Lett*. **2009**, *9*, 2807.
(12) Hajduk, D. A.; Takenouchi, H.; Hillmyer, M. A.; Bates, F. S.; Vigild, M. E.; Almdal, K. *Macromolecules* **1997**, *30*, 3788.
(13) Hajduk, D. A.; Ho, R.-M.; Hillmyer, M. A.; Bates, F. S.; Almdal, K. *J. Phys. Chem. B* **1998**, *102*, 1356.
(14) Jinnai, H.; Hasegawa, H.; Nishikawa, Y.; Sevink, G. J. A.; Braunfeld, M. B.; Agard, D. A.; Spontak, R. J. *Macromol. Rapid Commun*. **2006**, *27*, 1424.
(15) Schulz, M. F.; Bates, F. S.; Almdal, K.; Mortensen, K. *Phys. Rev. Lett*. **1994**, *73*, 86.
(16) Forster, S.; Khandpur, A. K.; Zhao, J.; Bates, F. S.; Hamley, I. W.; Ryan, A. J.; Bras, W. *Macromolecules* **1994**, *27*, 6922.
(17) Wang, C. Y.; Lodge, T. P. *Macromolecules* **2002**, *35*, 6997.
(18) Wang, C. Y.; Lodge, T. P. *Macromol. Rapid Commun*. **2002**, *23*, 49.
(19) Sakurai, S.; Umeda, H.; Furukawa, C.; Irie, H.; Nomura, S.; Lee, H. H.; Kim, J. K. *J. Chem. Phys*. **1998**, *108*, 4333.
(20) Hamley, I. W.; Fairclough, J. P. A.; Ryan, A. J.; Mai, S.-M.; Booth, C. *Phys. Chem. Chem. Phys*. **1999**, *1*, 2097.
(21) Sakamoto, N.; Hashimoto, T. *Macromolecules* **1998**, *31*, 3292.
(22) Chastek, T. Q.; Lodge, T. P. *Macromolecules* **2003**, *36*, 7672.
(23) Dair, B. J.; Avgeropoulos, A.; Hadjichristidis, N.; Capel, M.; Thomas, E. L. *Polymer* **2000**, *41*, 6231.
(24) Ho, R.-M.; Chiang, Y.-W.; Tsai, C.-C.; Lin, C.-C.; Ko, B.-T.; Huang, B.-H. *J. Am. Chem. Soc*. **2004**, *126*, 2704.
(25) Chiang, Y.-W.; Ho, R.-M.; Ko, B.-T.; Lin, C.-C. *Angew. Chem., Int. Ed*. **2005**, *44*, 7969.
(26) Ho, R.-M.; Chen, C.-K.; Chiang, Y.-W.; Ko, B.-T.; Lin, C.-C. *Adv. Mater*. **2006**, *18*, 2355.
(27) Chiang, Y.-W.; Ho, R.-M.; Thomas, E. L.; Burger, C.; Hsiao, B. S. *Adv. Funct. Mater*. **2009**, *19*, 448.
(28) Tseng, W.-H.; Chen, C.-K.; Chiang, Y.-W.; Ho, R.-M.; Akasaka, S.; Hasegawa, H. *J. Am. Chem. Soc*. **2009**, *131*, 1356.
(29) Ho, R.-M.; Chen, C.-K.; Chiang, Y.-W. *Macromol. Rapid Commun*. **2009**, *30*, 1439.
(30) Ho, R.-M.; Chiang, Y.-W.; Chen, C.-K.; Wang, H.-W.; Hasegawa, H.; Akasaka, S.; Thomas, E. L.; Burger, C.; Hsiao, B. S. *J. Am. Chem. Soc*. **2009**, *131*, 18533.
(31) Zalusky, A. S.; Olayo-Valles, R.; Wolf, J. H.; Hillmyer, M. A. *J. Am. Chem. Soc*. **2002**, *124*, 12761–12773.
(32) Kim, G.; Libera, M. *Macromolecules* **1998**, *31*, 2569.
(33) Zhang, Q.; Tsui, O. K. C.; Du, B.; Zhang, F.; Tang, T.; He, T. *Macromolecules* **2000**, *33*, 9561.
(34) Mareau, V. H.; Akasaka, S.; Osaka, T.; Hasegawa, H. *Macromolecules* **2007**, *40*, 9032.
(35) Park, H. W.; Jung, J.; Chang, T.; Matsunaga, K.; Jinnai, H. *J. Am. Chem. Soc*. **2009**, *131*, 46.
(36) Matsen, M. W. *Phys. Rev. Lett*. **1998**, *80*, 4470.
(37) Honda, T.; Kawakatsu, T. *Macromolecules* **2006**, *39*, 2340.
(38) Pinna, M.; Zvelindovsky, A. V. *Soft Matter* **2008**, *4*, 316.
(39) Hajduk, D. A.; Harper, P. E.; Gruner, S. M.; Honeker, C. C.; Kim, G.; Thomas, E. L.; Fetter, L. J. *Macromolecules* **1994**, *27*, 4063.
(40) Epps, T. H., III; Cochran, E. W.; Bailey, T. S.; Waletzko, R. S.; Hardy, C. M.; Bates, F. S. *Macromolecules* **2004**, *37*, 8325.